In vivo imaging of vessel diameter, size, and density: a comparative study between MRI and histology.

Benjamin Lemasson, Samuel Valable, Régine Farion, Alexandre Krainik, Chantal Rémy, Emmanuel L. Barbier

In vivo imaging of vessel diameter, size and density: a comparative study between MRI and histology

LEMASSON Benjamin, PhD[1,2], VALABLE Samuel, PhD[1,2,4], FARION Régine[1,2], KRAINIK Alexandre, MD PhD[1,2,3], REMY Chantal, PhD[1,2], BARBIER Emmanuel L., PhD[1,2*]

[1]Inserm, U836, Grenoble, F-38042, France

[2]Université Joseph Fourier, Grenoble Institut des Neurosciences, UMR-S836, Grenoble, F-38042, France

[3]Centre Hospitalier Universitaire de Grenoble, Département de Neuroradiologie et MRI, SFR1, Grenoble, F-38042, France

[4]CERVOxy team "Hypoxia and cerebrovascular pathophysiology", UMR 6232 CI-NAPS; Université de Caen Basse-Normandie; Université Paris-Descartes; CNRS; CEA. Centre Cyceron, CAEN, France.

*Corresponding author:
Emmanuel L. BARBIER
Grenoble Institut des Neurosciences – U836
Team 5 «Functional NeuroImaging and Brain Perfusion»
UJF Site santé – BP 170
38042 Grenoble cedex 9
Tel: 33 4 56 52 05 88 / Fax: 33 4 56 52 05 98
emmanuel.barbier@ujf-grenoble.fr

word count: 3577

keywords: perfusion, brain, microvasculature, USPIO, glioma, MRI

Running title: Vessel diameter, size and density: MRI vs histology

Abstract

The aim of this study was to compare MRI and histological estimates of the mean vessel diameter (mVD), the vessel density (Density), and the vessel size index (VSI) obtained in the same tumor-bearing animals.

Twenty-seven rats bearing intracranial glioma (C6 or RG2) were imaged by MRI. Changes in transverse relaxations (R_2* and R_2) were induced by the injection of an iron-based contrast agent and were mapped using a multi gradient-echo spin-echo sequence. Then, brain vascular network was studied *ex vivo* by histology. Three regions of interest were drawn in apparently normal tissue (neocortex and striatum) and in the tumor. *In vivo* mVD_{MRI}, $Density_{MRI}$, and VSI_{MRI} were measured; *ex vivo*, mVD_{histo}, $Density_{histo}$, and VSI_{histo} were quantified on the same animals.

MRI and histology measurements differed by -15 to 26%. A positive correlation was found between MRI and histology for mVD, Density, and VSI counterparts (R^2=0.62, 0.50, 0.73, respectively; $p<0.001$ in all cases). This study indicates that MRI and histology yields well correlated estimates of mVD, Density, and VSI. VSI is the closest MRI estimate to histology. As Density and mVD or VSI provide complementary information, it is worth computing them to characterize angiogenesis beyond blood volume fraction.

Words: 196/200

Keywords: perfusion, brain, microvasculature, USPIO, glioma, MRI

Introduction

The assessment of angiogenesis contributes to determining tumor grade and prognosis (1-3) for brain tumor suffering patients. In clinical practice, one estimates the microvessel density from surgical biopsies (4). This invasive approach yields the angiogenic features of a small part of the tumor but remains the only approved approach for tumor grading by WHO. In case of a heterogeneous high grade tumor, this characterization is not sufficient (5). *In vivo* imaging of angiogenic features is therefore very desirable.

To characterize angiogenesis *in vivo* with MRI, one usually maps the blood volume fraction (BVf) using a bolus tracking approach (6). On the one hand, BVf increases with the number of microvessels within an imaging voxel. On the other hand, BVf may remain constant in case of microvessel diameter increase and vessel density decrease (7), and thus becomes blind to angiogenic processes. This lack of BVf sensitivity to fully characterize angiogenesis is well-known by anatomopathologists who rather use the microvessel density (8). From a physical point of view, vessel density may be seen as a combination between microvessel diameter and BVf (9).

Using MRI, one may also image angiogenesis beyond BVf. This involves measuring the changes in transverse relaxivities induced by the injection of an intravascular contrast agent: changes in R_2 (noted ΔR_2 and measured using spin-echoes) and in R_2* (noted ΔR_2* and measured using gradient-echoes). Due to the sensitivity of MRI to water diffusion (ADC), ΔR_2 depends on the vessel diameter while ΔR_2* does not (10). Three processing approaches have then been proposed. All rely on some symplifying assumptions (small BVf, intravoxel microvessels modeled by perfect cylinders, statistical analysis of the intravoxel microvessel distribution, signals

measured in the static dephasing regime) (9-17). (**i**) Dennie *et al*. introduced $\Delta R_2^*/\Delta R_2$ as a non-quantitative estimate of the mean vessel diameter in the voxel (mVD_{MRI}) (11, 12); (**ii**) Based on $(\Delta R_2)^3/(\Delta R_2^*)^2$, Jensen *et al*. derived an estimate of the microvessel density ($Density_{MRI}$) (9, 13, 14); (**iii**) Based on $(\Delta R_2^*/\Delta R_2)^{3/2}$, Tropres *et al*. defined a quantitative index of the distribution of microvessel diameters within the voxel, the vessel size index (VSI_{MRI}) (15-17). VSI accounts for the influence of ADC on ΔR_2. These three methods have been applied in humans (9, 12, 16, 18) and a few validation studies have been conducted (7, 11, 13, 17, 19). They have not been evaluated together on the same dataset, however. How do they compare to histology and which approach should be used to characterize angiogenesis beyond BVf?

In this study, we compare MRI and histological estimates of the mVD, Density, and VSI. For this purpose, we used data collected on rat bearing orthotopic C6 and RG2 gliomas at four growth stages, two glioma models which present differences in their microvasculature (7). Note that the data regarding tumor evolution, including observations on angiogenic factors, have already been described in (7).

Methods

Animal manipulations

The study design was approved by the local committee for animal care and use (approval 081). Experiments were performed under permits n° 380508, A3851610004 and B3851610003 from the French Ministry of Agriculture. All experiments were performed under anesthesia: 5% isoflurane for induction, 2 % for maintenance in 70 % air / 30 % oxygen. Rectal temperature was maintained at 37.0 ± 0.5°C throughout the experiments.

Tumor cell implantation

Male Wistar (175-200 g, n=15) and Fischer 344 (150-175 g, n=12) rats were used for the C6 and RG2 high grade glioma models, respectively. The cell suspension (1.10^5 C6 cells (ATCC, CCL-107); 5.10^3 RG2 cells (ATCC, CRL-223)) was injected in the right striatum as described in (20).

Each animal was imaged once by MRI and euthanized immediately after for histology. The C6 model was imaged 11 (n=4), 15 (n=4), 20 (n=4) and 25 days (n=3) after tumor implantation and the RG2 model 6 (n=3), 10 (n=4), 14 (n=2) and 18 days (n=3) after tumor implantation. In both cases, the last time point corresponds to about 3 days prior to mean survival time (unpublished data) allowing the development of angiogenesis in both cases and thereby the exploration of a large range of microvascular characteristics.

In vivo MRI experiments

Experiments were performed on a horizontal 2.35 Tesla (40 cm diameter) magnet equipped with actively shielded gradient coils (Magnex Scientific Ltd., Oxford, UK) and interfaced to a SMIS console (SMIS Ltd, Guildford, UK). After anesthesia, the tail vein was equipped with a catheter. 200 µl of plasma were obtained (plasma "before injection").

Maps of Apparent Diffusion Coefficient (ADC) of water were computed from 3 diffusion-weighted spin-echo images (in X, Y, and Z directions) with b = 900 $s.mm^{-2}$ and a reference image (b ≈ 0 $s.mm^{-2}$) (voxel size = 234x454x1000 μm^3). A multi gradient-echo and spin-echo MRI sequence (TR = 6 s, 7 evenly spaced gradient-echoes = [6-42] ms, 1 spin-echo = 102 ms, voxel size = 234x454x1000 μm^3) was acquired just prior to and 4 min after administration of Sinerem® via the tail vein in about 20 sec (200 µmoles of iron/kg body weight) (Sinerem®, Guerbet SA, France; Combidex®, Advanced Magnetics, Inc, USA). Sinerem® is a dextran coated ultrasmall super-paramagnetic iron oxide (USPIO) contrast agent of about 20 nm in size and 4.5 hours plasma half-life (17). This USPIO does not significantly extravasate in these tumor models within the duration of our MRI protocol (7, 21). At the end of the MRI experiments, 200 µl of plasma "after injection" was obtained. Per animal, the total MRI session lasted 1h20min.

Plasma iron concentration determination

The plasma samples "before injection" and "after injection" were diluted 8 and 20 times with saline, respectively. T_2 measurements were performed on these diluted plasma samples using a Carr-Purcell-Meiboom-Gill sequence (400 echoes; echo spacing = 0.9 ms and 8 ms for plasma samples collected after and before injection

respectively) (22). A mono-exponential decay was fitted to the data to determine T_2. Plasma iron concentrations were eventually obtained from the measured T_2 values using $[Fe] = 0.01056_x(1/T_2) - 0.00024$ (equation determined in (7)).

Histology

At the end of the MRI experiment, rats were decapitated. Brains were quickly removed, frozen in -40°C isopentane and stored at -80°C and sliced at -20°C with a cryostat (20 µm thick sections).

Vascular structures in brains were detected post-mortem by immunohistochemistry of collagen IV. Collagen IV is a constituent of the basal lamina and can thus be used to delineate the microvascular contours. Sections were rehydrated in phosphate-buffered saline (PBS, 0.01M), fixed in 4% paraformaldehyde. After saturation in PBS-Tween 0.01%-BSA 3% for 1 h at room temperature, a goat antibody directed against collagen IV (Southern Biotech, USA) was incubated overnight at 4°C in PBS-Tween 0.01%-BSA 1% and the revelation was performed using an Alexa 546-linked Donkey anti-goat IgG (Invitrogen, France). At the end of the process, slices were counterstained with Hoescht 33342. Adjacent sections were stained with hematoxylin-eosin (HE) in order to delineate the tumor.

Data Processing

Region of interest (ROI): Three ROIs (contralateral striatum, contralateral neocortex, and tumor) were delineated on the slice (ADC map for MRI and HE section for histology) containing the largest tumor area. The ROI "tumor" corresponded to the region of increased ADC for the C6 model and to the region of apparently reduced

ADC for the RG2 model. Each ROI, delineated on the ADC map, was transferred onto the ΔR_2, ΔR_2*, mVD_{MRI}, $Density_{MRI}$, and VSI_{MRI} maps.

For histological data, the ROI "tumor" corresponded to the region of high cell density and was reported on the collagen-IV labeled section.

Computation of mVD_{MRI}, $Density_{MRI}$, and VSI_{MRI}: Changes in transverse relaxation rates due to USPIO (ΔR_2* and ΔR_2) and ADC values were obtained pixelwise as previously reported (17). Voxels for which the analysis could not be performed (i.e. non converging fit and values outside the range of validity of the method (ADC>3000 $\mu m^2.s^{-1}$; $\Delta R_2^* \leq 0$; $\Delta R_2 \leq 0$)) were marked as excluded. Rejected voxels represented 2.5% and 1.9% of the total number of voxels for the C6 and RG2 models, respectively. For each ROI, mean ADC, ΔR_2*, and ΔR_2 values were computed. Then, mVD_{MRI} was computed as:

$$mVD_{MRI} = \frac{\Delta R_2^*}{\Delta R_2} \quad [1]$$

$Density_{MRI}$ was computed using Eq. [7] from ref (13):

$$Density_{MRI} = 329 \frac{(\Delta R_2)^3}{(\Delta R_2^*)^2} \quad [2]$$

VSI_{MRI} was computed using Eq. [14] from (17)

$$VSI_{MRI} = 0.424 \left(\frac{ADC}{\gamma \Delta \chi B_0} \right)^{1/2} \left(\frac{\Delta R_2^*}{\Delta R_2} \right)^{3/2}, \quad [3]$$

where ADC was computed as the mean of the ADCs observed in the three principal directions of the gradient system; B_0 and γ represent the static magnetic field and the gyromagnetic ratio of the protons. Based on Eq. [13] from (17), the increase in blood magnetic susceptibility due to USPIO, $\Delta\chi$, was derived using three different approaches:

(**i**) $\Delta\chi$ was considered equal to 0.57 ppm (17).

(**ii**) ΔR_2* was measured in the contralateral neocortex. In (17), Eq. [3] describes the link between $\Delta\chi$ and BVf. This equation may be modified to derive $\Delta\chi$, assuming a constant contralateral BVf_{contra} of 3%:

$$\Delta\chi = \frac{3}{4\pi}\frac{\Delta R^*_{2,contra}}{BV\,\mathrm{f}_{contra}\gamma B_0}. \qquad [4]$$

(**iii**) $\Delta\chi$ was derived animal per animal from the difference in plasma iron concentrations measured before and after injection of USPIO, knowing the saturation magnetization of USPIO and the static magnetic field values (17).

Quantitative histological analysis: Sections (3 slices per animal located around the largest size of the tumor mass and 3 microscopic fields per ROI and per slice) were digitized using a CCD camera (Olympus, France). The background noise was low enough to perform image analysis. Analysis of blood vessels was performed automatically using NIH ImageJ software (http://rsb.info.nih.gov/ij/). The photographs of blood vessels were binarized by local thresholding at the half-height. Fractional vascular surface was computed as the surface occupied by vessels. The vessel diameter was derived from the "Morphology-Particles8 plus" plugin. To allow comparison between MR and histological estimates, mean vessel diameter (mVD_{histo}), mean vessel density ($Density_{histo}$), fractional vascular surface, and mean vessel length were derived. Based on these histological estimates, VSI_{histo} was derived as described in (17).

Propagation of errors

To evaluate the relative sensitivity of mVD_{MRI}, $Density_{MRI}$ and VSI_{MRI} to errors, the equations for error propagation were derived starting from Eqs [1-3], assuming each

contribution independent (Appendix). Errors were evaluated for $\Delta R_2 \in [5, 25]$ ms, $\Delta R_2^* \in [20, 90]$ ms, ADC=700 µm²/s and $\Delta\chi$=0.60ppm. The two latter values are the mean values found this study and the ΔR_2 and ΔR_2* ranges correspond to what was observed in this study. Note that the procedure was applied on ROIs but could be similarly apply on individual pixels.

Statistical analysis

Paired student *t*-tests were used for neocortex/striatum and for tumor/striatum comparisons. Unpaired student *t*-tests were used to compare C6 and RG2 tumors. The Pearson correlation coefficient was computed to evaluate:

- whether mVD_{histo}, $Density_{histo}$, and VSI_{histo} obtained on all ROIs and all animals are predictors of mVD_{MRI}, $Density_{MRI}$, and VSI_{MRI}, respectively;
- which estimate of $\Delta\chi$ yields the best correlation between VSI_{histo} and VSI_{MRI}.

All results are expressed as mean ± SD.

The effects of time and tumor model were evaluated with an ANOVA, using Bonferroni correction for multiple comparisons, for each MRI microvascular estimates (mVD_{MRI}, $Density_{MRI}$, and VSI_{MRI}).

Results

Impact of $\Delta\chi$ and ADC on VSI_{MRI} estimates

The three approaches used to compute $\Delta\chi$ yielded the following correlations between VSI_{MRI} and VSI_{histo}: R^2=0.70 for the constant $\Delta\chi$; R^2=0.74 for the $\Delta\chi$ obtained considering a constant contralateral BVf and R^2=0.73 for the $\Delta\chi$ obtained from estimated USPIO concentration in each animal ($p<0.001$ in all cases; data not shown). This result is in line with a variable $\Delta\chi$ across injections (cf. Table 1), due to inter-animal or inter-species variability and to limited accuracy on the injected volume. To remain consistent with previously published results (7), $\Delta\chi$ measured animal by animal was used in the subsequent analysis. We also observed that using a constant ADC in Eq. [3] (like in (17), where ADC=700 $\mu m^2.s^{-1}$ was used) instead of the measured ADC reduces the R^2 from 0.73 to 0.71 ($p<0.001$). Using both a constant ADC and a constant $\Delta\chi$ led to R^2=0.64 ($p<0.001$).

Mean estimates of mVD, Density and VSI

Figure 1 shows examples of MRI maps and histological field of views of one representative animal of each model. Table 1 shows the estimates derived from MRI and from histology for the three ROIs in Wistar and Fischer rats (averaged across all animals in each case). Striatum and neocortex yield similar estimates for both MRI and histology (except in Wistar rats for whom the $Density_{histo}$ was 14% lower in the striatum than in the neocortex). For both MRI and histology, the standard deviation in non-tumoral ROIs (an estimate of the reproducibility) was better than 20%, except for $Density_{MRI}$ for which the standard deviation increases up to 50% (31% on average). As the tumor evolves over time, the standard deviation measured in the tumor is larger than in the contralateral tissue. Estimates obtained in the tumor ROIs were

different from those obtained in the striatum (except for ADC in the RG2 model). Both tumors exhibited larger vessel diameters (higher VSI and mVD) and lower Density than the contralateral striatum. All MRI and histological estimates were able to differentiate C6 from RG2, except mVD_{MRI}.

Errors on mVD_{MRI}, $Density_{MRI}$ and VSI_{MRI}

As Eqs. [1-3] are a mixture of additions, products, and powers, the relative errors on mVD_{MRI}, $Density_{MRI}$, and VSI_{MRI} are constants if the relative errors on ΔR_2, ΔR_2*, ADC, $\Delta\chi$ are also constant. Setting the relative errors on ΔR_2 and ΔR_2* to 10 and 15% (reproducibility observed in the laboratory) and the relative errors on ADC and $\Delta\chi$ to 0 led to an error on mVD_{MRI}=18.0%, $Density_{MRI}$=49.2% and VSI_{MRI}=27.0%. Note that for errors on mVD_{MRI} and VSI_{MRI}, the relative contributions of the errors on ΔR_2 and ΔR_2* are equivalent. This is not the case for $Density_{MRI}$ for which the contribution of the error on ΔR_2 is 1.5 that of the error on ΔR_2*. If the relative error on ΔR_2 is only 10%, then the relative error on $Density_{MRI}$ becomes 36.1%. For VSI, two additional parameters are used: ADC and $\Delta\chi$. When the relative errors on ADC and $\Delta\chi$ are set to 10% instead of 0, the relative error on VSI_{MRI} becomes 27.9%.

MRI versus histology

Figure 2 shows the correlation between the three MRI estimates and their corresponding histological estimates for all ROIs and all animals (data from both tumor models were pooled). A positive correlation is obtained for the three microvascular characteristics studied *in vivo* and *ex vivo*: mVD (Fig. 2a), Density (Fig. 2b), and VSI (Fig. 2c). The lowest correlation between MRI and histology is obtained for Density (R^2=0.50, $p<0.001$). The correlation between mVD_{MRI} and mVD_{histo} is better (R^2=0.62, $p<0.001$) and the best correlation is found between VSI_{MRI} and VSI_{histo} (R^2=0.73, $p<0.001$). One also found a very good correlation between mVD

and VSI (R^2=0.79 between MRI estimates; R^2=0.76 between histological estimates; data not shown; $p<0.001$ in both cases). Bland-Altman graphs (Fig. 3) reveal a slight bias between MRI and histology for all estimates (26% for mVD; 13% for Density; -15% for VSI). Note that for mVD, the bias is computed between an amount computed in arbitrary unit (mVD_{MRI}) and an amount expressed in µm (mVD_{histo}) and as such may not be interpreted as the bias obtained for Density and VSI. A trend appears for VSI: MRI overestimates histology as VSI increases. In all cases, more than 90% of the data are within the range mean ± 2 standard-deviations, however.

Temporal evolution of microvascular characteristics

Figure 4 shows the temporal evolution of mVD_{MRI}, $Density_{MRI}$, and VSI_{MRI} in C6 and RG2 tumors and in the contralateral striatum. In the striatum, these three estimates appear robust (low SD), except for $Density_{MRI}$ in the Wistar rats which exhibits higher SD. From a statistical point of view (Table 2), no time and no model effect was observed for the striatum, except for VSI_{MRI} which differs between Wistar and Fischer rats. In both tumor types, mVD_{MRI} and VSI_{MRI} increases as tumor evolves, while $Density_{MRI}$ decreases. In the tumor, a time and a model effects are observed for the three MRI estimates, except for mVD_{MRI} whose evolution is comparable between the two models.

Discussion

In this study, three MRI estimates derived from the changes in R_2 and R_2* consecutive to the injection of USPIO are compared to their histological counterparts using data collected on rats bearing orthotopic C6 and RG2 gliomas. A positive correlation was found between *in vivo* and *ex vivo* measurements of the three metrics. Our results indicate that MRI mapping of the mVD, Density, and VSI may be used to characterize tumor angiogenesis well beyond BVf.

Both tumors exhibited the same evolution pattern: an increase in vessel diameter associated to a decrease in vessel density. This evolution pattern does not imply a change in BVf. In (7), it was shown that BVf remains stable over time for the C6 model while it increases for the RG2 model. Thus, one should be cautious when using BVf as sole characteristic of angiogenesis.

Microvascular estimates obtained in normal brain (averaged across neocortex and striatum and across all animals) are in good agreement with previously reported values. Dennie *et al*. reported a mVD_{MRI} of 4.8±0.3 a.u. in the rat brain (11), while we observed 3.7±0.6 a.u. Wu *et al.* reported a $Density_{MRI}$ of 282±43 vessel.mm^{-2} in the mouse brain (13), while we observed 271 ± 83 vessel.mm^{-2}. Tropres *et al.* reported a VSI_{MRI} of 4.5±0.8 µm in the rat brain (17), while we observed 4.2±0.9 µm. Regarding error propagation, one can notice that the variabilities obtained in this study for mVD_{MRI}, $Density_{MRI}$, and VSI_{MRI} (16%, 31%, and 21% respectively) are lower than the errors obtained from the propagation analysis (18.0%, 49.2%, and 27.9% respectively), suggesting a possible mechanism of error compensation during data processing.

Numerous factors may bias histological and MRI measurements. First, histological estimates are based on the analysis of all vessels while MRI estimates rely on vessels perfused by the contrast agent. In histology, freezing may induce a tissue expansion, cryosectioning a tissue compression (23) and measuring the external diameter of objects stained with a pan-vascular marker like Collagen IV may yield an overestimation of the vessel diameter. The stereological extrapolation of surface to volume parameters has limited accuracy because of the underlying assumption that vessels are perfect cylinders. Also, a 20 µm-thick histological slice does not accurately represent a 1 mm-thick MRI slice across a heterogeneous tumor. MRI estimates may be biased by the difference between the spatial configuration of real vessels (especially in a tumor) in the voxels used in this study and the idealized configuration (perfect cylinders, large number of vessels, voxel size) used in modeling (24, 25) or by macroscopic magnetic field heterogeneities. In the present study, none of the quantitative data available – alone or combined – may explain the differences in absolute values observed in Figure 3. Further studies are needed for a finer validation of the MRI measurements, including numerical simulations to evaluate the impact of the assumptions of the model (such as voxel size, oxygen saturation, microvascular organization, presence of myelin...).

The lower correlation between MRI and histology values obtained for Density could be ascribed in part to the lower accuracy on $Density_{MRI}$ obtained in this study. This lower accuracy arises from the noise level which was higher on ΔR_2 than on ΔR_2* and from the fact that $Density_{MRI}$ is more sensitive to the noise on ΔR_2 than to the noise on ΔR_2* while mVD and VSI are similarly sensitive to the noise on ΔR_2 and on

ΔR_2*. Despite this lower accuracy on $Density_{MRI}$, similar bias between MRI and histology were found for Density and VSI (less than 15% in both cases). From a correlation point of view, the better correlation coefficient obtained between MRI and histological estimates of VSI compared to those obtained for mVD and Density could be ascribed in part to the more careful quantification performed in Eq. [3]: the computation of VSI includes the estimate of ADC (which varies between tumor and contralateral tissue) and of the actual contrast agent concentration (which has a variability above 24% in this study) while mVD and Density do not. Indeed, using a constant ADC and a constant contrast agent concentration reduces the correlation coefficient between MRI and histological estimates of VSI down to R^2=0.64, close to the value found for MRI and histological estimates of mVD (R^2=0.62) or between VSI_{MRI} and mVD_{Histo} (R^2=0.62). One can also observe that the additional error due to the use of ADC and $\Delta\chi$ is small (0.9% difference in error propagations). In case the actual contrast agent concentration may not readily be obtained (e.g. in a clinical setting), an estimate of the local contrast agent concentration obtained by considering a constant blood volume fraction in the contralateral region appears as a very good solution (similar correlations between MRI and histology estimates of VSI are obtained when using a measured $\Delta\chi$ and a $\Delta\chi$ estimated from the contralateral BVf).

In conclusion, this study indicates that MRI and histological estimates of mVD, Density, and VSI obtained on the same animals are well correlated and may be used to characterize angiogenesis *in vivo* beyond BVf. While the results obtained in this study were obtained using a USPIO and a steady-state approach, it has recently been shown that a dynamic approach using Gd-chelate yielded similar results to

those obtained with USPIO at steady-state (19, 26). A combination of blood volume fraction, Density, and VSI or mVD (the latter two are well correlated) appears thus desirable to improve the characterization of angiogenesis in patients.

Appendix

The error on mVD, εmVD, is given by:

$$(\varepsilon mVD)^2 = \left|\frac{\partial mVD}{\partial \Delta R_2}\right|^2 (\varepsilon \Delta R_2)^2 + \left|\frac{\partial mVD}{\partial \Delta R_2^*}\right|^2 (\varepsilon \Delta R_2^*)^2 \quad [A1]$$

where $\varepsilon \Delta R_2$ and $\varepsilon \Delta R_2^*$ are the errors on ΔR_2 and ΔR_2^* estimates, and with

$$\frac{\partial mVD}{\partial \Delta R_2} = -\frac{\Delta R_2^*}{(\Delta R_2)^2} \quad [A2]$$

$$\frac{\partial mVD}{\partial \Delta R_2^*} = \frac{1}{\Delta R_2} \quad [A3]$$

The error on Density, $\varepsilon Density$, is given by:

$$(\varepsilon Density)^2 = \left|\frac{\partial Density}{\partial \Delta R_2}\right|^2 (\varepsilon \Delta R_2)^2 + \left|\frac{\partial Density}{\partial \Delta R_2^*}\right|^2 (\varepsilon \Delta R_2^*)^2 \quad [A4]$$

with

$$\frac{\partial Density}{\partial \Delta R_2} = 329.3.\frac{(\Delta R_2)^2}{(\Delta R_2^*)^2} \quad [A5]$$

$$\frac{\partial Density}{\partial \Delta R_2^*} = -329.2.\frac{(\Delta R_2)^3}{(\Delta R_2^*)^3} \quad [A6]$$

The error on VSI, εVSI, is given by:

$$(\varepsilon VSI)^2 = \left|\frac{\partial VSI}{\partial \Delta R_2}\right|^2 (\varepsilon \Delta R_2)^2 + \left|\frac{\partial VSI}{\partial \Delta R_2^*}\right|^2 (\varepsilon \Delta R_2^*)^2 + \left|\frac{\partial VSI}{\partial ADC}\right|^2 (\varepsilon ADC)^2 + \left|\frac{\partial VSI}{\partial \Delta \chi}\right|^2 (\varepsilon \Delta \chi)^2 \quad [A7]$$

where εADC and $\Delta\chi$ are the errors on *ADC* and $\Delta\chi$ estimates, respectively, and with

$$\frac{\partial VSI}{\partial \Delta R_2} = -0.424.\frac{3}{2}.\left(\frac{ADC}{\gamma.\Delta\chi.B_0}\right)^{1/2}.\frac{(\Delta R_2^*)^{3/2}}{(\Delta R_2)^{5/2}} \quad [A8]$$

$$\frac{\partial VSI}{\partial \Delta R_2^*} = 0.424.\frac{3}{2}.\left(\frac{ADC}{\gamma.\Delta\chi.B_0}\right)^{1/2}.\frac{(\Delta R_2^*)^{1/2}}{(\Delta R_2)^{3/2}} \quad [A9]$$

$$\frac{\partial VSI}{\partial ADC} = \frac{0.424}{2.(ADC)^{1/2}}.\left(\frac{1}{\gamma.\Delta\chi.B_0}\right)^{1/2}.\left(\frac{\Delta R_2^*}{\Delta R_2}\right)^{3/2} \quad [A10]$$

$$\frac{\partial VSI}{\partial \Delta \chi} = -\frac{0.424}{2}.\left(\frac{ADC}{\gamma.B_0}\right)^{1/2}.\left(\frac{\Delta R_2^*}{\Delta R_2}\right)^{3/2}.(\Delta\chi)^{-3/2} \quad [A11]$$

Acknowledgments

S.V. benefited from a post-doctoral grant from “La Ligue Contre le Cancer”.

The authors acknowledge the MRI facility of Grenoble for its experimental support, Guerbet for providing Sinerem®, the "Association pour la Recherche sur le Cancer", the “Institut National du Cancer”, the “Région Rhône-Alpes”, and the “Cancéropôle Lyon Auvergne Rhône-Alpes” for their financial support.

References

1. Burger PC, Vogel FS, Green SB, Strike TA. Glioblastoma multiforme and anaplastic astrocytoma. Pathologic criteria and prognostic implications. Cancer 1985;56(5):1106-1111.

2. Daumas-Duport C, Tucker ML, Kolles H, Cervera P, Beuvon F, Varlet P, Udo N, Koziak M, Chodkiewicz JP. Oligodendrogliomas. Part II: A new grading system based on morphological and imaging criteria. J Neurooncol 1997;34(1):61-78.

3. Daumas-Duport C, Varlet P, Tucker ML, Beuvon F, Cervera P, Chodkiewicz JP. Oligodendrogliomas. Part I: Patterns of growth, histological diagnosis, clinical and imaging correlations: a study of 153 cases. J Neurooncol 1997;34(1):37-59.

4. Takei H, Bhattacharjee MB, Rivera A, Dancer Y, Powell SZ. New immunohistochemical markers in the evaluation of central nervous system tumors: a review of 7 selected adult and pediatric brain tumors. Arch Pathol Lab Med 2007;131(2):234-241.

5. Folkman J. Role of angiogenesis in tumor growth and metastasis. Semin Oncol 2002;29(6 Suppl 16):15-18.

6. Wintermark M, Sesay M, Barbier E, Borbely K, Dillon WP, Eastwood JD, Glenn TC, Grandin CB, Pedraza S, Soustiel JF, Nariai T, Zaharchuk G, Caille JM, Dousset V, Yonas H. Comparative overview of brain perfusion imaging techniques. Stroke 2005;36(9):2032-2033.

7. Valable S, Lemasson B, Farion R, Beaumont M, Segebarth C, Remy C, Barbier EL. Assessment of blood volume, vessel size, and the expression of angiogenic factors in two rat glioma models: a longitudinal in vivo and ex vivo study. NMR Biomed 2008;21(10):1043-1056.

8. Hasan J, Byers R, Jayson GC. Intra-tumoural microvessel density in human solid tumours. Br J Cancer 2002;86(10):1566-1577.

9. Jensen JH, Lu H, Inglese M. Microvessel density estimation in the human brain by means of dynamic contrast-enhanced echo-planar imaging. Magn Reson Med 2006;56(5):1145-1150.

10. Boxerman JL, Hamberg LM, Rosen BR, Weisskoff RM. MR contrast due to intravascular magnetic susceptibility perturbations. Magn Reson Med 1995;34:555-566.

11. Dennie J, Mandeville JB, Boxerman JL, Packard SD, Rosen BR, Weisskoff RM. NMR imaging of changes in vascular morphology due to tumor angiogenesis. Magn Reson Med 1998;40:793-799.

12. Schmainda KM, Rand SD, Joseph AM, Lund R, Ward BD, Pathak AP, Ulmer JL, Badruddoja MA, Krouwer HG. Characterization of a first-pass gradient-echo spin-echo method to predict brain tumor grade and angiogenesis. AJNR Am J Neuroradiol 2004;25(9):1524-1532.

13. Wu EX, Tang H, Jensen JH. High-resolution MR imaging of mouse brain microvasculature using the relaxation rate shift index Q. NMR Biomed 2004;17(7):507-512.

14. Jensen JH, Chandra R. MR imaging of microvasculature. Magn Reson Med 2000;44(2):224-230.

15. Tropres I, Grimault S, Vaeth A, Grillon E, Julien C, Payen J, Lamalle L, Décorps M. Vessel Size imaging. Magn Reson Med 2001;45(3):397-408.

16. Kiselev VG, Strecker R, Ziyeh S, Speck O, Hennig J. Vessel size imaging in humans. Magn Reson Med 2005;53(3):553-563.

17. Tropres I, Lamalle L, Peoc'h M, Farion R, Usson Y, Decorps M, Remy C. In vivo assessment of tumoral angiogenesis. Magn Reson Med 2004;51(3):533-541.

18. Donahue KM, Krouwer HG, Rand SD, Pathak AP, Marszalkowski CS, Censky SC, Prost RW. Utility of simultaneously acquired gradient-echo and spin-echo cerebral blood volume and morphology maps in brain tumor patients. Magn Reson Med 2000;43(6):845-53.

19. Farrar CT, Kamoun WS, Ley CD, Kim YR, Kwon SJ, Dai G, Rosen BR, di TE, Jain RK, Sorensen AG. In vivo validation of MRI vessel caliber index measurement methods with intravital optical microscopy in a U87 mouse brain tumor model. Neuro Oncol 2010;12(4):341-350.

20. Valable S, Barbier EL, Bernaudin M, Roussel S, Segebarth C, Petit E, Remy C. In vivo MRI tracking of exogenous monocytes/macrophages targeting brain tumors in a rat model of glioma. Neuroimage 2008;40(2):973-983.

21. Beaumont M, Lemasson B, Farion R, Segebarth C, Remy C, Barbier EL. Characterization of tumor angiogenesis in rat brain using iron-based vessel size index MRI in combination with gadolinium-based dynamic contrast-enhanced MRI. J Cereb Blood Flow Metab 2009;29(10):1714-1726.

22. Meiboom S, Gill D. Modifed Spin Echo method of measuring nuclear relaxation times. The review of scientific instruments 1958;29(8):688-691.

23. Simonetti AW, Elezi VA, Farion R, Malandain G, Segebarth C, Remy C, Barbier EL. A low temperature embedding and section registration strategy for 3D image reconstruction of the rat brain from autoradiographic sections. J Neurosci Methods 2006;158(2):242-250.

24. Pathak AP, Ward BD, Schmainda KM. A novel technique for modeling susceptibility-based contrast mechanisms for arbitrary microvascular geometries: the finite perturber method. Neuroimage 2008;40(3):1130-1143.

25. Christen T, Zaharchuk G, Pannetier N, Serduc R, Joudiou N, Vial JC, Rémy C, Barbier EL. Quantitative MR estimates of blood oxygenation based on T2*: a numerical study of the impact of model assumptions. Magn Reson Med 2011;In Press.

26. Pannetier N, Lemasson B, Christen T, Tachrount M, Tropres I, Farion R, Segebarth C, Remy C, Barbier EL. Vessel size index measurements in a rat model of glioma: comparison of the dynamic (Gd) and steady-state (iron-oxide) susceptibility contrast MRI approaches. NMR Biomed 2011;Early view ahead of Print (DOI: 10.1002/nbm.1734).

Figure captions

Figure 1. MRI and histological images obtained from one representative animal of each model: (a) C6 and (b) RG2. The three ROIs used in this study are overlaid on the T_2-weighted images (blue: tumor, green: cortex and red: striatum). Excluded pixels are displayed in yellow.

Figure 2. Correlation between MRI and histological estimates of (**a**) mVD, (**b**) Density, and (**c**) VSI. A point corresponds to one ROI (contralateral striatum, contralateral neocortex or tumor) in one animal.

Figure 3. Bland-Altman plots comparing histological and MRI estimates of (**a**) mVD, (**b**) Density, and (**c**) VSI. A point corresponds to one ROI (contralateral striatum, contralateral neocortex or tumor) in one animal. The thick line corresponds to the mean difference between MRI and histological estimates and the thin dotted lines to two standard deviations.

Figure 4. Temporal evolution of mVD (**a**, **b**), Density (**c**, **d**), and VSI (**e**, **f**) for tumor (filled circles) and contralateral striatum (open squares) ROIs (average across animals).

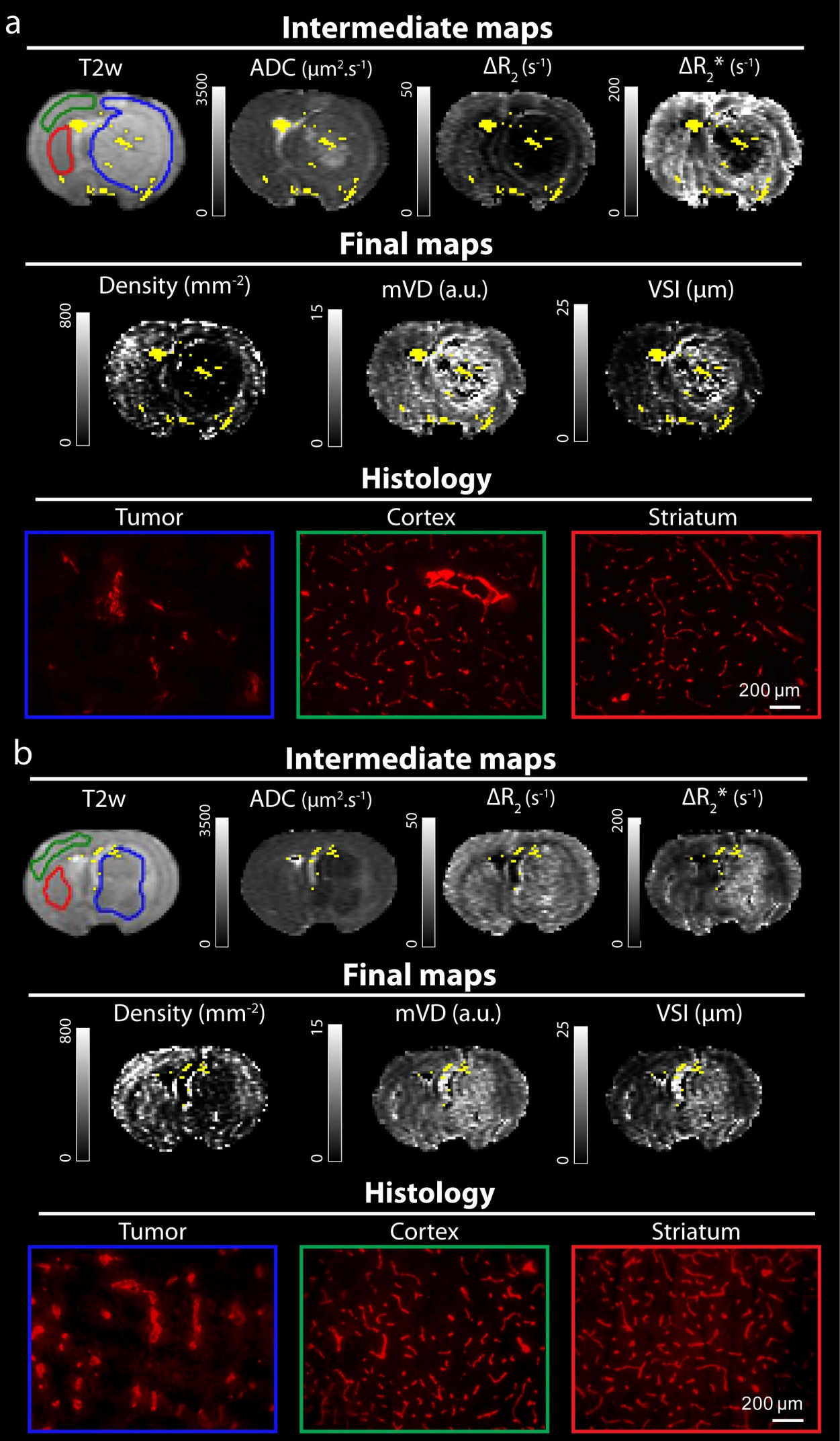
a
Intermediate maps
T2w
ADC (μm².s⁻¹)
3500
0
ΔR2 (s⁻¹)
50
0
ΔR2* (s⁻¹)
200
0
Final maps
Density (mm⁻²)
800
0
mVD (a.u.)
15
0
VSI (μm)
25
0
Histology
Tumor
Cortex
Striatum
200 μm
b
Intermediate maps
T2w
ADC (μm².s⁻¹)
3500
0
ΔR2 (s⁻¹)
50
0
ΔR2* (s⁻¹)
200
0
Final maps
Density (mm⁻²)
800
0
mVD (a.u.)
15
0
VSI (μm)
25
0
Histology
Tumor
Cortex
Striatum
200 μm

Figure 2.

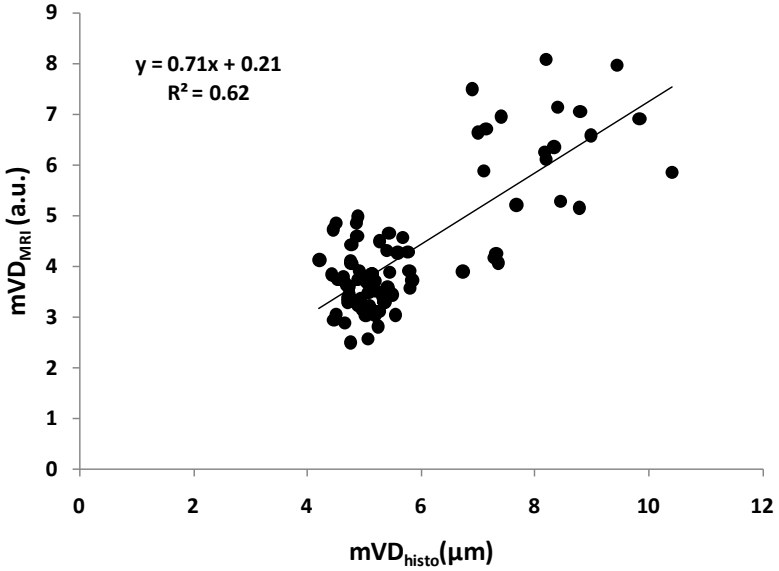
y = 0.71x + 0.21
R² = 0.62
mVD_MRI (a.u.)
mVD_histo(µm)

a

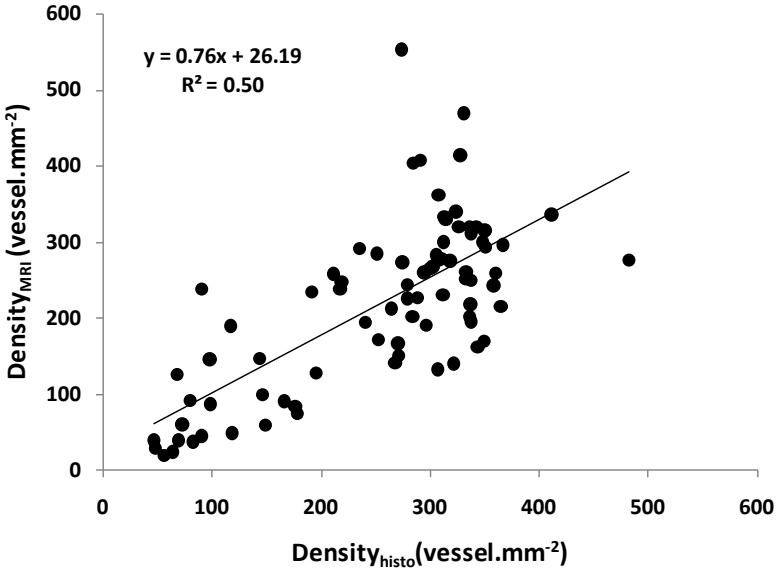
y = 0.76x + 26.19
R² = 0.50
Density_MRI (vessel.mm-2)
Density_histo(vessel.mm-2)

b

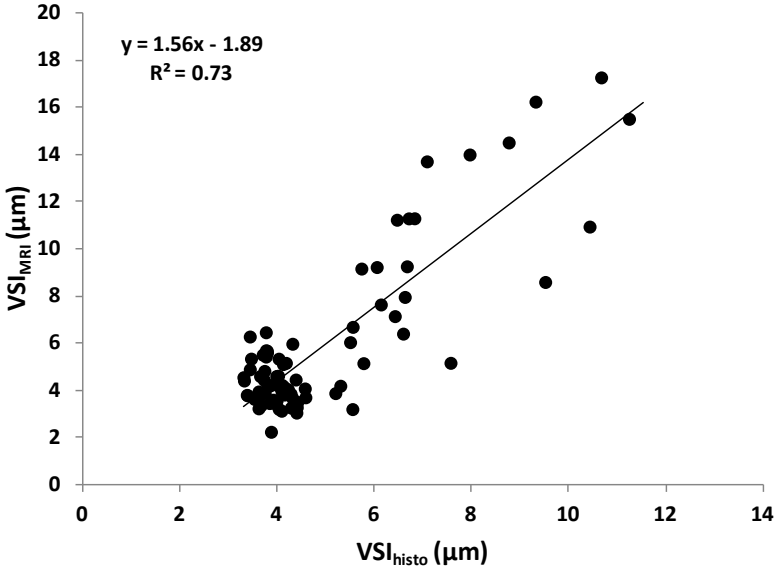
y = 1.56x - 1.89
R² = 0.73
VSI_MRI (µm)
VSI_histo (µm)

c

Figure 3.

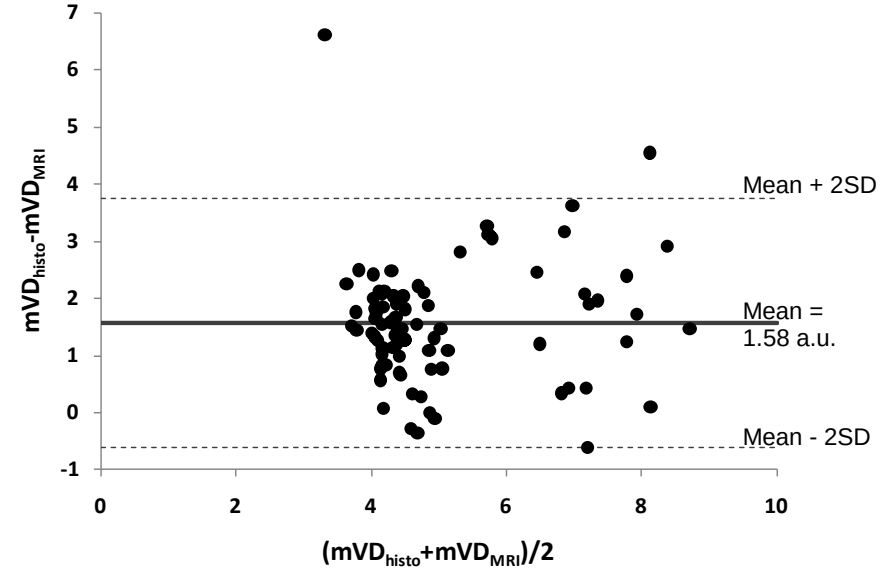
Mean + 2SD
Mean =
1.58 a.u.
Mean - 2SD
mVD_histo-mVD_MRI
(mVD_histo+mVD_MRI)/2

a

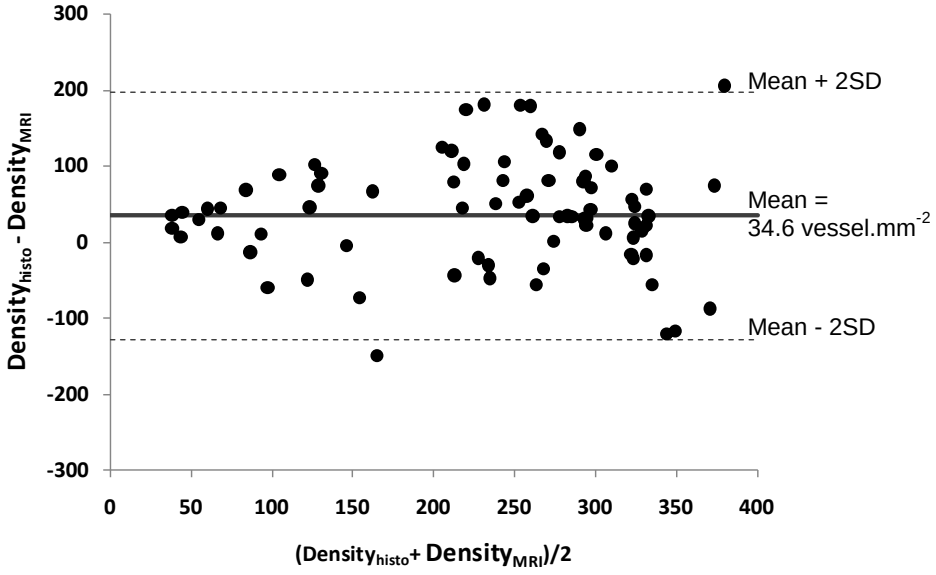
Mean + 2SD
Mean =
34.6 vessel.mm-2
Mean - 2SD
Density_histo - Density_MRI
(Density_histo+ Density_MRI)/2

b

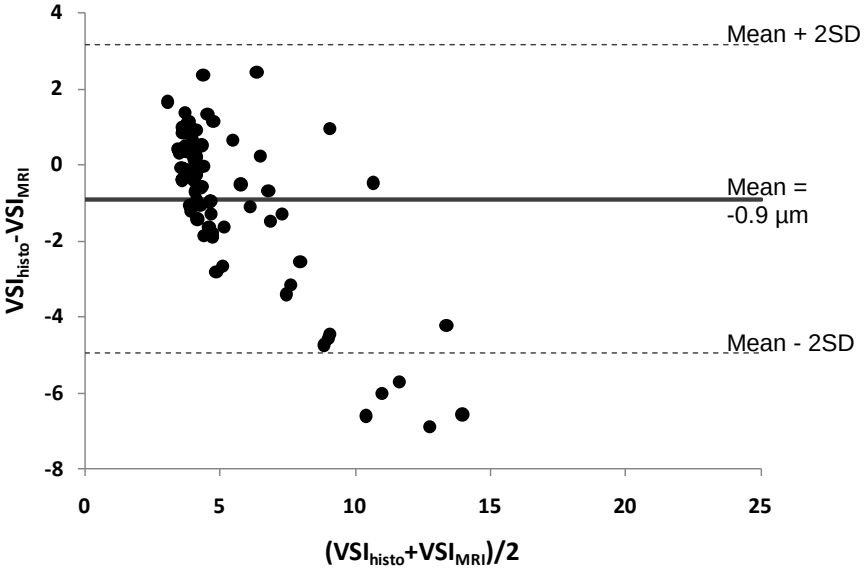
Mean + 2SD
Mean =
-0.9 µm
Mean - 2SD
VSI_histo-VSI_MRI
(VSI_histo+VSI_MRI)/2

c

Figure 4.

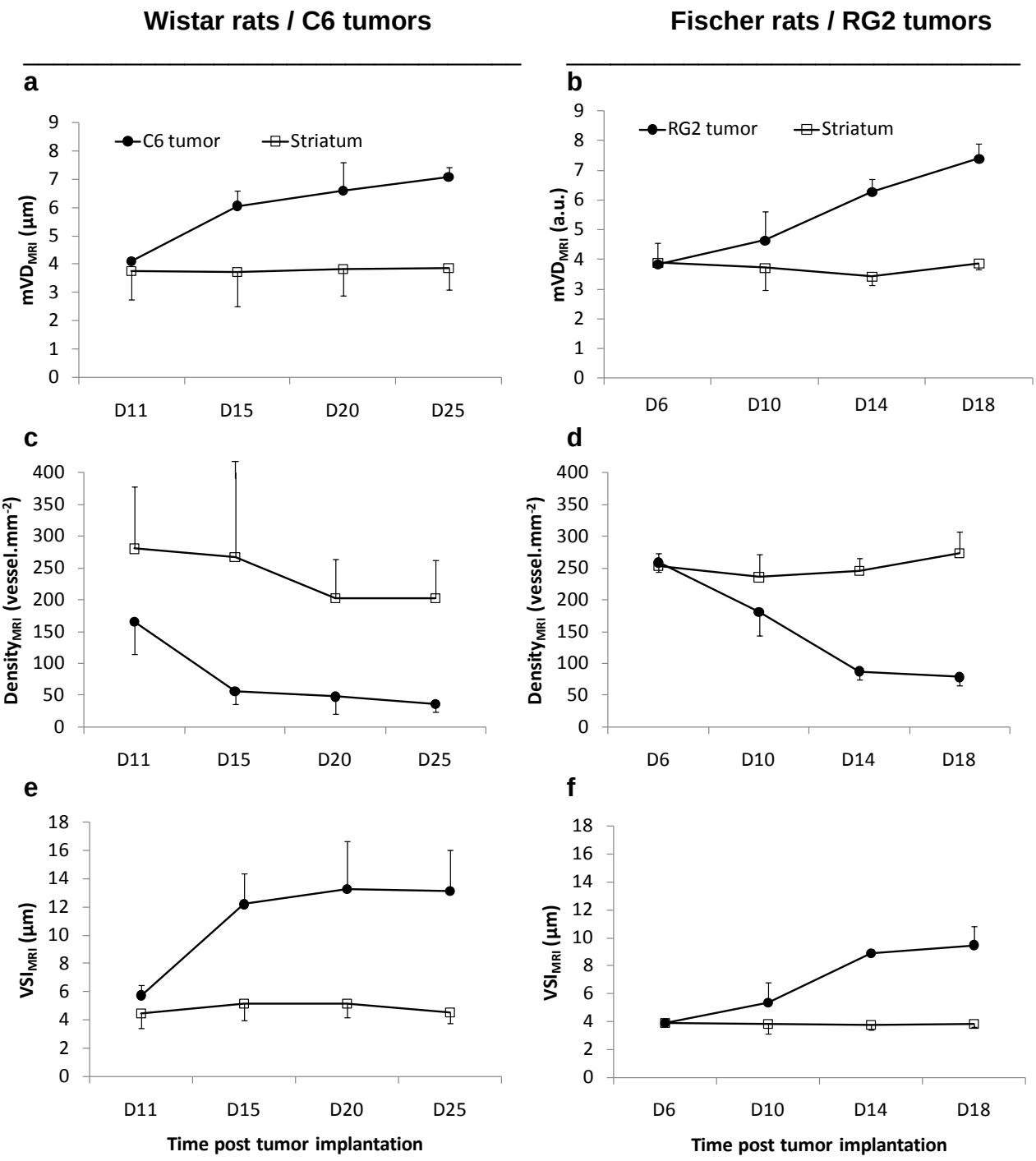
Wistar rats / C6 tumors
Fischer rats / RG2 tumors
a
b
c
d
e
f
C6 tumor
Striatum
RG2 tumor
Striatum
mVD_MRI (µm)
mVD_MRI (a.u.)
Density_MRI (vessel.mm-2)
VSI_MRI (µm)
D11
D15
D20
D25
D6
D10
D14
D18
Time post tumor implantation

Table 1. $\Delta\chi$ derived from change in iron plasma concentration for Wistar and Fisher rats, averaged across animals. MRI estimates (ADC, mVD_{MRI}, $Density_{MRI}$, VSI_{MRI}), and histological estimates (mVD_{histo}, $Density_{histo}$, VSI_{histo}) within the neocortex, the striatum, and the tumor of Wistar and Fischer rats. * p<0.05 between striatum and neocortex; $$ p<0.01 and $$$ p<0.001 between tumor and striatum; £ p<0.05, ££ p<0.01 and £££ p<0.001 between C6 and RG2 tumors.

	Wistar Rats (C6 model)			**Fischer Rats (RG2 model)**		
$\Delta\chi$ (ppm)	0.50 ± 0.15			0.71 ± 0.17		
	Neocortex	Striatum	Tumor	Neocortex	Striatum	Tumor
ADC ($\mu m^2.s^{-1}$)	724 ± 39	733 ± 40	919 ± 74$^{\$\$\$}$	675 ± 29	679 ± 32	651 ± 63$^{£££}$
mVD_{MRI} (a.u.)	3.5 ± 0.5	3.8 ± 0.8	5.9 ± 1.3$^{\$\$\$}$	3.7 ± 0.7	3.8 ± 0.4	5.4 ± 1.6$^{\$\$}$
$Density_{MRI}$ (vessel. mm^{-2})	294 ± 48	240 ± 115	79 ± 62$^{\$\$\$}$	300 ± 92	251 ± 34	159 ± 79$^{\$\$,££}$
VSI_{MRI} (µm)	4.4 ± 0.7	4.9 ± 1.1	10.9 ± 4.2$^{\$\$\$}$	3.7 ± 0.8	3.8 ± 0.5	6.6 ± 2.7$^{\$\$,££}$
mVD_{histo} (µm)	4.8 ± 0.3	4.8 ± 0.3	8.1 ± 1.0$^{\$\$\$}$	5.2 ± 0.3	5.3 ± 0.4	6.8 ± 1.5$^{\$\$,££}$
$Density_{histo}$ (vessel.mm^{-2})	343 ± 36	295 ± 61*	80 ± 26$^{\$\$\$}$	322 ± 22	303 ± 42	200 ± 59$^{\$\$\$,£££}$
VSI_{histo} (µm)	3.8 ± 0.2	4.0 ± 0.5	7.9 ± 2.1$^{\$\$\$}$	4.0 ± 0.3	4.0 ± 0.3	6.1 ± 1.6$^{\$\$,£}$

Table 2. Statistical evaluation of the effects of time and glioma model (C6 or RG2) on mVD_{MRI}, $Density_{MRI}$, VSI_{MRI}

	mVD_{MRI}			**$Density_{MRI}$**			**VSI_{MRI}**		
	time	model	time x model	time	model	time x model	time	model	time x model
Striatum	ns	ns	ns	ns	ns	ns	ns	p=0.02	ns
Tumor	p<0.001	ns	ns	p<0.001	p<0.001	p=0.07	p<0.001	p<0.001	ns